ARTICLE

Check for updates

Direct observation of Néel-type skyrmions and domain walls in a ferrimagnetic DyCo₃ thin film

Chen Luo[1,2], Kai Chen [1,3✉], Victor Ukleev[1], Sebastian Wintz[1,4], Markus Weigand [1,4], Radu-Marius Abrudan[1], Karel Prokeš[5] & Florin Radu [1✉]

Isolated magnetic skyrmions are stable, topologically protected spin textures that are at the forefront of research interests today due to their potential applications in information technology. A distinct class of skyrmion hosts are rare earth - transition metal (RE-TM) ferrimagnetic materials. To date, the nature and the control of basic traits of skyrmions in these materials are not fully understood. We show that for an archetypal ferrimagnetic material DyCo₃ that exhibits a strong perpendicular anisotropy, the ferrimagnetic skyrmion size can be tuned by an external magnetic field. Moreover, by taking advantage of the high spatial resolution of scanning transmission X-ray microscopy (STXM) and utilizing a large x-ray magnetic linear dichroism (XMLD) contrast that occurs naturally at the RE resonant edges, we resolve the nature of the magnetic domain walls of ferrimagnetic skyrmions. We demonstrate that through this method one can easily discriminate between Bloch and Néel type domain walls for each individual skyrmion. For all isolated ferrimagnetic skyrmions, we observe that the domain walls are of Néel-type. This key information is corroborated with results of micromagnetic simulations and allows us to conclude on the nature of the Dzyaloshinskii-Moriya interaction (DMI) which concurs to the stabilisation of skyrmions in this ferrimagnetic system. Establishing that an intrinsic DMI occurs in RE-TM materials will also be beneficial towards a deeper understanding of chiral spin texture control in ferrimagnetic materials.

[1] Helmholtz-Zentrum-Berlin für Materialien und Energie, Albert-Einstein-Straße 15, 12489 Berlin, Germany. [2] Institute of Experimental Physics of Functional Spin Systems, Technical University Munich, James-Franck-Straße 1, 85748 Garching b München, Germany. [3] National Synchrotron Radiation Laboratory, University of Science and Technology of China, 230029 Hefei, Anhui, China. [4] Max-Planck-Institut für Intelligente Systeme, 70569 Stuttgart, Germany. [5] Helmholtz-Zentrum-Berlin für Materialien und Energie, Hahn-Meitner Platz 1, 14109 Berlin, Germany. ✉email: kaichen2021@ustc.edu.cn; florin.radu@helmholtz-berlin.de

Magnetic skyrmions are stable nanoscale whirls of magnetic spin textures[1–6]. Due to their topological stability, small size at the nanometer scale and controlled mobility under low current densities, skyrmions hold the promise to impact significantly next-generation information storage technology[7–16]. Initially introduced in nuclear physics as soliton solutions of non-linear field equations[1,17], they hold now a distinct place in solid state physics as well, following their theoretical prediction[18] and experimental observation[19]. Broken inversion symmetry that is characteristic to certain crystal structures induces a non-collinear coupling mechanism that contributes as an asymmetric term in the Hamiltonian describing the resulting magnetically chiral ground states[20]. Under certain conditions, these chiral states concur in forming magnetic skyrmions as observed in archetypal cubic chiral crystals that exhibit a bulk Dzyaloshinskii-Moriya interaction (DMI)[19,21–25]. Moreover, symmetry breaking along with spin-orbit coupling present at magnetic interfaces lead to a weak interfacial DMI that contributes to the stabilisation of skyrmions observed in thin films[26–30] and multilayers[31–36].

Skyrmion lattices that occur in single crystals fill a small pocket in the phase diagram for temperatures that typically extends over few Kelvin[19,37]. This is detrimental to applications which require stability over a broad range around room temperature. The temperature pocket can be eventually extended by reducing the dimensionality of the structures or by engineering the interfacial DMI of ferromagnetic thin films and multilayers[38]. Yet, caused by the skyrmion Hall effect[39,40], the trajectories of these ferromagnetic topological units in devices are not straight, being deflected away by the Lorentz forces. To overcome this limitation, ferrimagnetic materials are offering an advantage due to a versatile tunability of their magnetic properties.

Rare earth transition metals (RE-TM) ferrimagnetic (FiM) alloys consist of two anitferromagnetically coupled sublattices. At the compensation temperature (T_{comp}), the magnetizations of both sub-lattices are equal, leading to a vanishing net magnetization, just as for an antiferromagnet. By the choice of the elemental composition and through temperature variation, their magnetic properties, including T_{comp}, net magnetization and magnetic anisotropy, can be easily engineered, which makes FiM materials advantageous for spintronics devices[41–43]. By selecting the RE element, two classes of FiM can be distinguished, namely Gd-base FiM alloys that exhibit a weak perpendicular magnetic anisotropy (PMA) due to the vanishing orbital moment of the RE, and Dy, Tb, Ho-based FiM alloys which have a stronger PMA due to the large orbital moment of the RE. The latter category has the potential to offer a higher stability of stored information, but the reports on skyrmions in these systems are scarce[44].

By contrast, for weak PMA FiM alloys, like FeGdCo, magnetic skyrmions have been recently observed[45] and they can be controlled in microstructured devices[46,47]. Since then, much research has been carried out to enable control and fuctionalization of ferrimagnetic skyrmions: they have been observed in ferrimagnetic confined nanostructures[48]; topological spin memory is reported for Co/Gd multilayers exhibiting skyrmion stability in fully compensated antiferromagnetically coupled heterostructure[49]; observation of spin spirals and individual skyrmions in synthetic Pt/CoGd/Pt ferrimagnetic multilayers at room-temperature has been achieved without the assistance of external magnetic fields[50]; magneto-transport measurements have revealed a topological contribution resulting from the occurrence of an interfacial DMI in Ho/CoFeGd/β-W multilayers[51]; evidence for chiral ferrimagnetism in an ultrathin GdCo layer has been demonstrated through a combination of high-resolution Lorentz microscopy and XMCD[52]; Néel-type homochirality has been observed over a large temperature range in Ta/Ir/Fe/GdFeCo/Pt multilayers using scanning electron microscopy with polarization analysis[53]; and information

on Néel versus Bloch DWs can be inferred by a tilt geometry with Lorentz transmission microscopy as shown for a Mn_3Sn topological antiferromagnet[54]. However, a direct determination of the type of the spin structures, namely Néel-type versus Bloch-type, was not experimentally reported, for neither of the two FiM classes.

An unambiguous determination of the skyrmion type is crucial for understanding the stabilization mechanism of skyrmions in these materials. Indeed, one would expect stabilization of Néel-type skyrmions in a thin film system with an interfacial DMI induced by engineering of the spin–orbit coupling of the ferrimagnetic layer with neighboring heavy-metal (HM) layers[8]. However, this approach usually requires stacking ultrathin magnetic and HM layers into an asymmetric periodic multilayer in order to achieve a sizeable magnitude of DMI and, consequently, a small enough (~100 nm) skyrmion size[32]. On the other hand, "bulk" DMI stabilizing chiral Bloch-type skyrmions requires an intrinsic lack of inversion symmetry within the material[20]. Alternatively, skyrmion bubbles having the same topological charge, but degenerate chirality can also be stabilized by dipolar interactions[55]. Furthermore, dipolar interaction can compete with an interfacial DMI and change the spin rotation sense from Néel to Bloch type, or give rise to hybrid spin textures[56]. Therefore, unveiling the skyrmion type in FiM will shed light onto the microscopic spin Hamiltonian in this class of thin-film FiM alloys.

In this study, we report real space imaging of the magnetic structures in a FiM $DyCo_3$ thin film by means of scanning transmission x-ray microscopy (STXM), utilizing both x-ray magnetic circular dichroism (XMCD) and x-ray magnetic linear dichroism (XMLD) contrast[57–61]. Using XMCD-STXM, we directly observe well-isolated FiM skyrmions and their transformation to maze-like domains as a function of an out-of-plane external field. With XMLD-STXM, we demonstrate that these FiM skyrmions are Néel-type and the maze-like domains also show a preference of Néel-type domain walls. We confirm our experimental results to be consistent with micromagnetic simulations. Please note that the experiments reported here are performed at low temperatures (26 K) which correspond to a non-fully compensated magnetization state. The fully compensated magnetization for this ferrimagnet occurs at a temperature that is well above the room temperature, therefore a vanishing skyrmion Hall effect is not addressed (see Supplementary Note 1.2).

Results and discussion

Field dependence of Skyrmion size. In Fig. 1a, we show the hysteresis loop in perpendicular geometry which was measured by SQUID magnetometry. The magnetic reversal of the $DyCo_3$ film as a function of applied field was investigated at 26 K using STXM. Because the maximum magnetic field for the STXM experiments is limited to 260 mT, which is not enough to saturate the sample at low temperatures, we saturated the sample out-of-plane at room temperature prior to the STXM measurements. After cooling down the sample (in a perpendicular magnetic field of +260 mT) to 26 K, the STXM images were obtained with the magnetic field sweeping from +260 to −260 mT. Figure 1b shows selected examples of XMCD-STXM areal images of the FiM skyrmions acquired at different perpendicular magnetic fields. One can distinguish the evolution of well-isolated FiM skyrmions as a function of the magnetic field, ranging from 260 to 140 mT (within the field range that is marked by a gray rectangle in Fig. 1a). The average density and radius of the skyrmions extracted from the STXM images as a function of field are shown in Fig. 1c, d, respectively. It increases from 2.5 to 9.6 skyrmions per square micrometer when the field is decreased from 260 to 140 mT, indicating that the skyrmions can be created and annihilated by varying the field. At the same time, the average
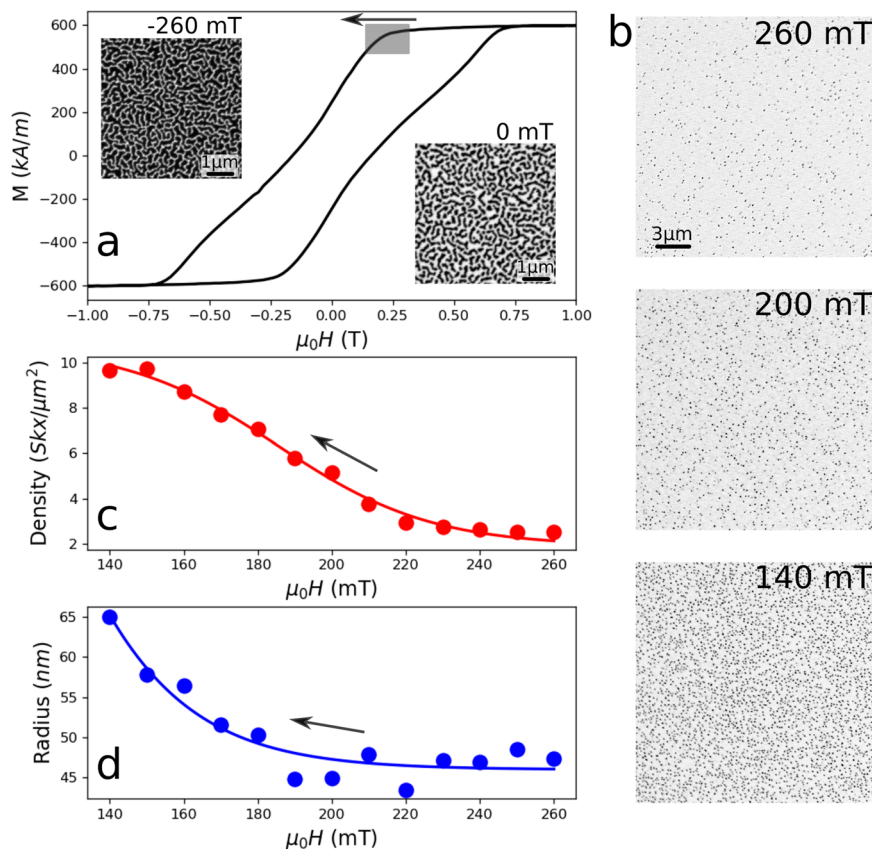
Fig. 1 Hysteresis loop (measured by superconducting quantum interference device (SQUID) magnetometry) and scanning transmission x-ray microscopy (STXM) images of ferrimagnetic (FiM) skyrmions at 26 K. a Out-of-plane magnetic hysteresis loop measured at 26 K by SQUID magnetometry. The external magnetic field $\mu_0 H$ is expressed in units and sub-units of Tesla (T), with μ_0 being the vacuum magnetic permeability and H denoting the magnetic field strength. **b** STXM images showing the FiM skyrmions at different perpendicular magnetic fields recorded at the Dy M_5 edge and 26 K. The average density (**c**) and radius (**d**) of the skyrmions as a function of external magnetic fields, were extracted from the STXM images. The gray rectangle box in (**a**) represents the magnetic field range where the FiM skyrmions are probed. The arrow represents the field sweeping direction. The insets of (**a**) show the transition into maze-like domains.

skyrmion radius R increases from 45 to 65 nm, demonstrating that the skyrmion size can be reduced and inflated with the external field. When the magnetic field decreases further, the skyrmions will merge into worm- and maze-like domain structures, as shown in the insets of Fig. 1a.

Lateral imaging of skyrmions with XMCD contrast. To resolve the details of the FiM skyrmions, high resolution XMCD-STXM images were recorded at the Co L_3 and the Dy M_5 edges at an external field of 140 mT, as shown in Fig. 2. The left panels display the images of several single skyrmions, whereas in the right panels we show their line profiles along the X and Y axes, which represent the normalized perpendicular magnetic moment of Dy (M_{Dy}) and Co (M_{Co}) elements. One can easily observe that the magnetic profiles of M_{Dy} and M_{Co} overlap nicely, which clearly demonstrate the formation of FiM skyrmions with an antiparallel alignment of the Dy and Co moments. At this field, the radius (FWHM) of the respective skyrmion is about 65 nm.

Lateral imaging of skyrmion domain walls with XMLD contrast. To identify the spin structure of the domain walls of the FiM skyrmions, XMLD was utilized by taking advantage of the strong linear dichroism of Dy at the M_5 absorption edge. Figure 3a presents the demonstration of x-ray absorption spectroscopy (XAS) at the Dy M_5 edge for circular left (CL), circular right (CR), linear vertical (LV) and linear horizontal (LH)

polarizations, respectively. The XMCD spectrum was obtained by taking the difference of (CR-CL), and the XMLD spectrum was obtained by taking the difference of (LV-LH). One can see that the maximum XMLD signal appears enhanced at the second peak of the Dy M_5 edge whereas the maximum XMCD signal is located at the third peak. The intensity of the XMLD spectra at the Dy edge is sufficiently large to be exploited for the STXM measurements[61]. Unlike XMCD which is sensitive to the magnetic moments collinear to the x-ray propagation direction, XMLD is sensitive to the magnetic moments collinear to the $\vec{E}$ vector of linearly polarized x-rays, which lies in the plane of the sample surface for our experimental geometry. To distinguish Néel-type and Bloch-type skyrmions from each other, we made simulations on how the two different types of skyrmions should look like in the presence of circular and linearly polarized x-rays, which are shown in Fig. 3b, c. By comparison, one can see that our experimental data match very well with the Néel-type contrast, indicating that the FiM skyrmions in our DyCo$_3$ thin film are Néel-type skyrmions.

Lateral imaging of domain walls of a maze domain state with XMLD contrast. After successfully identifying Néel-type skyrmions utilizing the advantage of XMLD, we also investigated the domain walls for maze-like domains using the same technique, as shown in Fig. 4a–c. One can easily observe that the domain walls at the top/bottom sides are more pronounced for LV, and that the
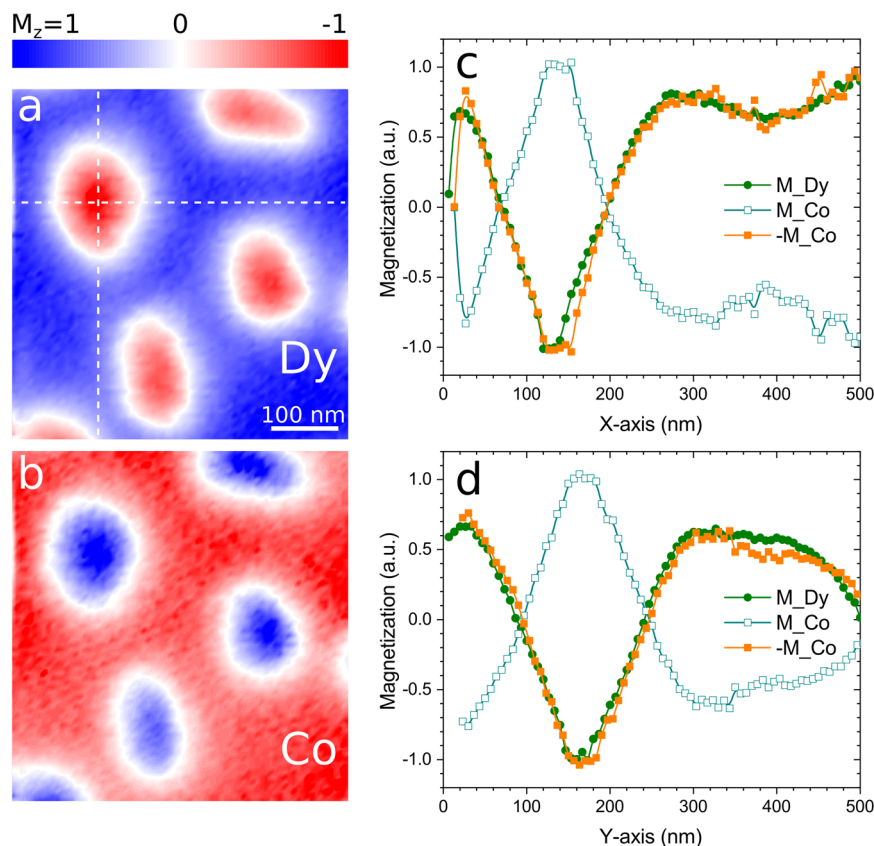
Fig. 2 X-ray magnetic circular dichroism imaging of isolated skyrmions. a Scanning transmission x-ray microscopy (STXM) images at the Co L_3 edge and the Dy M_5 edge (**b**), respectively. The color bar represents the normalized sublattice magnetization (M_z) along the magnetic field (and the x-ray beam) direction. **c**, **d** Line profiles across a skyrmion along the X and Y axes (see the dashed lines in (**a**)), representing the normalized perpendicular magnetic moment for Dy and Co elements.
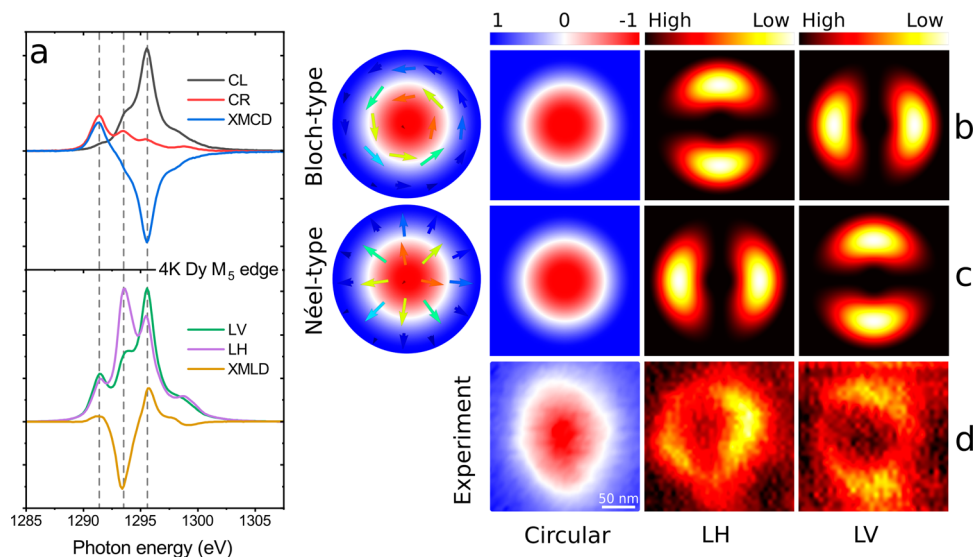
Fig. 3 Resolve of the magnetic domain wall type using x-ray magnetic linear dichroism. a X-ray absorption spectra (XAS) measured by circular left (CL), circular right (CR), linear horizontal (LH) and linear vertical (LV) polarized x-rays, as well as x-ray magnetic linear dichroism (XMLD) and x-ray magnetic circular dichroism(XMCD) spectra at the Dy M_5 edge at 4 K. The three peaks of the Dy M_5 edge are marked by dashed lines. Expected magnetic image contrast when using circular, LH and LV polarized x-rays for Bloch-type (**b**) and Néel-type (**c**) skyrmions. **d** Experimental Scanning transmission x-ray microscopy (STXM) results. Here the STXM images for LV and LH x-ray polarizations were obtained at the middle peak of the Dy M_5 edge, and the STXM image for circular polarized x-rays was measured at the third peak of the Dy M_5 edge.
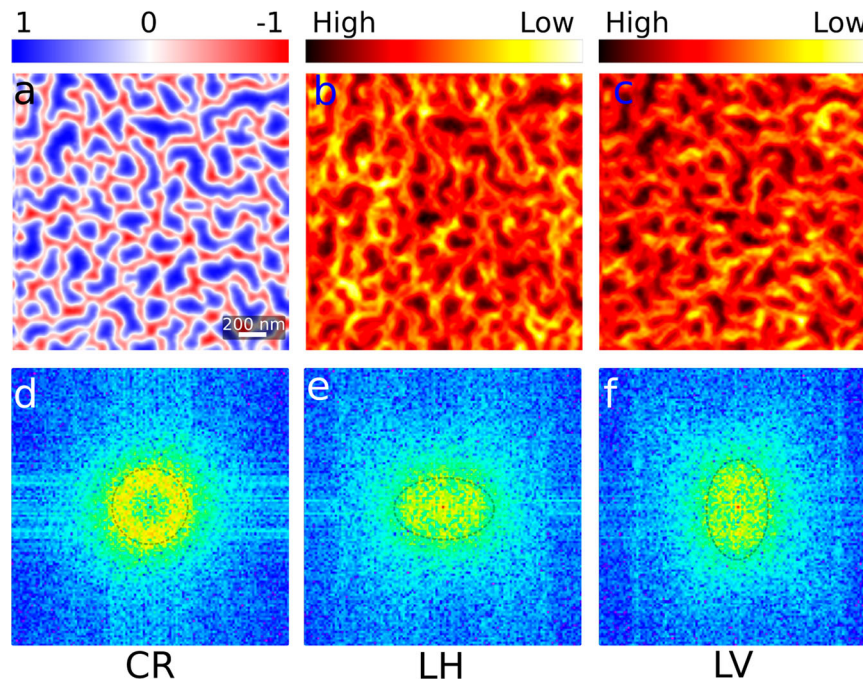
Fig. 4 Imaging of the magnetic domains and domain walls in a maze domain state and their corresponding Fast Fourier Transform. a–c Scanning transmission x-ray microscopy (STXM) images of the maze domains at -260 mT for circular right (CR), linear horizontal (LH) and linear vertical (LV) polarized x-rays, respectively. **d–f** Fast Fourier Transform (FFT) of the top STXM images, with the dashed circles and ellipses as guide to the eye.

domain walls at the left/right sides show more intensity for LH, similar to the domain walls in skyrmions shown in Fig. 3d. Note that, one still can see a weak contrast for some domain walls which do not follow this rule. This result indicates that the majority of the domain walls for maze-like domains are Néel-type with a low mixing of Bloch-type. We also applied Fast Fourier Transform (FFT) to the STXM images, which show different patterns for different polarizations (see Fig. 4d–f. The FFT shows a ring pattern for circular polarization. For linear polarization, however, it shows an ellipse with long vertical axis for LV and an ellipse with long horizontal axis for LH, which represent the preference of Néel-type domain walls (compare also to the results of micromagnetic simulations shown in the Supplementary Notes 3 and 4).

Micromagnetic simulations. Micromagnetic simulations were performed using the MuMax3 package[62] using magnetic parameters for a $DyCo_3$ thin film deduced in a previous study[44] and in the present magnetometry measurements that can be found in the Supplementary Information file (see Supplementary Note 1.1).

Figure 5 shows simulated magnetic structures as a function of the magnetic field applied perpendicular to the sample plane. The top row shows the color-coded three-dimensional orientation of the magnetization, and the bottom row shows the in-plane component M_x. A maze domain pattern shows up upon a relaxation of the random magnetization state at zero field (Fig. 5a), featuring also some Néel-type skyrmions with opposite polarities. Skyrmions with core magnetization parallel to the applied magnetic field collapse and disappear upon increasing the field (Fig. 5b). Finally, at a higher field of $\mu_0 H = 530$ mT the maze domain pattern evolves into a isolated skyrmion phase (Fig. 5c). This phase persists up to 810 mT when the skyrmions collapse and the sample gets fully magnetized along the field. Bottom panels of Fig. 5a–d show the in-plane magnetization component within each cell of the simulation. The contrast inversion from blue (left) to red (right) of each stable Néel-type skyrmion represents the chirality of the system given by the sign of the DMI constant, which is not picked up by the STXM experiment. Importantly, the simulation captures

accurately the impact of the domain wall type on the polarization-dependent STXM contrast. Circular and elliptic shapes of FFT patterns in Fig. 4d–f correspond very well to the ones calculated from the simulations (compare to Supplementary Fig. 7) described in the Supplementary Note 3.

Interestingly, the simulated skyrmion size is very tunable and can be changed by the external magnetic field by a factor of three from $R = 32$ nm at 530 mT to $R = 9$ nm at 810 mT. While the skyrmion size differs from the experimental value quite significantly, lower DMI parameters do not allow to stabilize purely Néel-type skyrmions but rather hybrid ones that carry Bloch caps at the surface (see Supplementary Note 5.2), being consistent with the theory reported for magnetic multilayers[63]. If no DMI is assumed, the interplay between PMA and the stray field results in the formation of a bubble lattice with dominantly Bloch-type domain walls (see Supplementary Note 5.1). Once a DMI term of sufficient strength is introduced, the stability of the skyrmions is increased towards higher fields, and the unique rotation sense of the domain walls gets defined. Note also that besides the DMI strength, the saturation net magnetization and the magnetic anisotropy parameters play an important role for the skyrmion formation in this material (see Supplementary Fig. 3).

For a discussion on the possible origin of a "bulk" DMI in this system, see ref. [44] and the afferent Supplementary Note 6. Similar observations have recently been reported in Fe_3GeTe_2 flakes of various thickness where an interplay between dipolar and DM interactions results in a complex history-dependent magnetic phase diagram of spin textures[64].

Conclusions

We presented an experimental resolve of skyrmion traits in a ferrimagnetic $DyCo_3$ thin film at 26 K using STXM imaging, utilizing both XMCD and XMLD contrast. With XMCD-STXM, the magnetic structures in real space are revealed as a function of decreasing external field. Well-isolated ferrimagnetic skyrmions are observed between $+260$ and $+140$ mT, and the density as well as the radius of the skyrmions can be controlled by the external
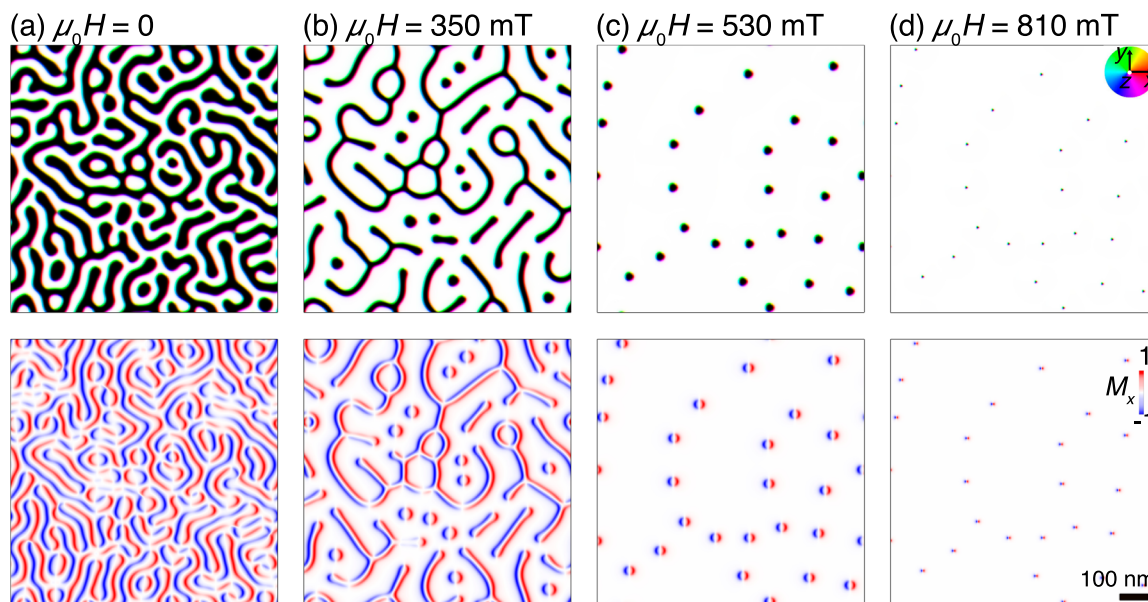
Fig. 5 Micromagnetic simulations demonstrating Néel-type skyrmion formation in the presence of a finite Dzyaloshinskii–Moriya interaction. Top row of (**a**–**d**): Micromagnetic simulations of relaxed spin configurations for the DyCo$_3$ film as a function of out-of-plane magnetic field. The external magnetic field $\mu_0 H$ is expressed in sub-units of Tesla (T), with μ_0 being the vacuum magnetic permeability and H denoting the magnetic field strength. The white and black colors represent the net normalized magnetization being parallel and antiparallel to the z-axis, respectively. The other colors represents the orientation of the in-plane component of the net magnetization within each cell as shown in the color wheel in top panel (**d**). Bottom row of (**a**–**d**): the magnetization component along the x-axis. The color bar shown in the bottom panel (**d**) represents the normalized net magnetization M_x.

magnetic field. When the magnetic field is further reduced, these skyrmions will merge into maze-like domains, which matches very well with the results of magnetic simulations. Utilizing XMLD-STXM at the Dy M$_5$ edge, we successfully identify the domain wall type of ferrimagnetic skyrmions to be of Néel-type. Moreover, the domain walls for the maze-like domains are also investigated, revealing also a majority of Néel-type domain walls. Hence, we are able to unambiguously conclude the interfacial-type symmetry[65] of DMI in DyCo$_3$ thin film. Nevertheless, the origin of the strong DMI of this type remains an open question. The technique of using XMLD contrast in the STXM measurements at the rare earth M edges provides a promising way to study complex spin textures in real-space, which is highly useful for the characterization of skyrmions, chiral domain walls and various non-collinear magnetic systems.

Methods
Sample preparation and characterization. The ferrimagnetic DyCo$_3$ film of 50 nm thickness was prepared by magnetron sputtering chamber (MAGSSY) at room temperature and in an argon atmosphere of 1.5×10^{-3} mbar with a base pressure of 5×10^{-9} mbar. The stoichiometry of the DyCo$_3$ alloy was controlled by varying the deposition rates of the Co and the Dy targets in a co-sputtering scheme. A Si$_3$N$_4$ membrane with a thickness of 100 nm was used as substrate for the soft x-ray transmission measurements. A capping layer of 3 nm-thick Ta was deposited on top of the sample surface to prevent surface oxidation. The magnetic properties of the sample have been measured by SQUID magnetometry and by anomalous Hall effect (Tensormeter RTM1, HZDR Innovation, Germany), and they are described in the Supplementary Information file.

X-ray measurements. Scanning transmission x-ray microscopy (STXM) measurements were performed at the MAXYMUS endstation at the Bessy II electron storage ring operated by the Helmholtz-Zentrum Berlin für Materialien und Energie[66]. The

x-ray beam was focused with a zone plate and an order selecting aperture on the transmissive sample in the presence of an applied out-of-plane magnetic field which was controlled by varying the arrangement of four permanent magnets. The STXM images were collected pixel by pixel using a piezoelectric sample stage at the Co L$_3$ edge and the Dy M$_5$ edge by exploiting the effects of x-ray magnetic circular dichroism (XMCD) and x-ray magnetic linear dichroism (XMLD). The XMLD contrast represents an intensity map for LV (vertical axis in real space, parallel to the sample surface) and LH (horizontal axis in real space, parallel to the sample surface) orientations of the linear polarization axes. When the linear polarization is perpendicular to the spin axis, the XAS intensity measured at the middle resonance peak of the M5 edge is low (high in transmission), whereas for a parallel orientation of the linear polarization axis with respect to the spin axis, the intensity is high (low in transmission) (see for instance Fig. S1, in ref. [61]). This makes the XMLD contrast easy to comprehend for the present transmission geometry of films with perpendicular magnetic anisotropy: a change of intensity along the linear direction shown on the LV, LH and L45 maps (see Supplementary Note 2) can be given only by Néel walls, whereas a change of intensity towards a direction perpendicular to the linear polarization direction can be given only by Bloch walls. Note that the experimental XMLD maps shown in the manuscript are all logarithm of the raw data images.

The XAS, XMLD and XMCD spectra for the Dy M$_5$ edge (Fig. 3a) were performed at the Deimos beamline at synchrotron Soleil[67] in transmission mode using the same 50 nm-thick DyCo$_3$ sample grown on a Si$_3$N$_4$ membrane. The magnetic field of 2 T, which is much higher than the saturation field, was applied along the beam during the XMCD measurements using circular polarized x-rays and perpendicular to the beam during the XMLD measurements using linear horizontal and linear vertical polarized x-rays.

Magnetic simulations. Micromagnetic simulations were performed using MuMax3[62]. The simulations were performed on a three-dimensional grid $512 \times 512 \times 25$ voxels with the size of

$2 \times 2 \times 2 \, \text{nm}^3$. The material parameters used for the simulation are given further below and can be found in the Supplementary Information file. A larger scale simulation with a grid of $1024 \times 1024 \times 25$ voxels was carried out for the simulation without DMI, in order to account for the larger domain size. The computation was performed using a graphics processing unit (GPU) NVIDIA GeForce RTX 3080 Ti. The following material parameters were used: exchange stiffness $A_{\text{ex}} = 6 \, \text{pJ m}^{-1}$, saturation magnetization $M_{\text{s}} = 600 \, \text{kA m}^{-1}$, and uniaxial anisotropy $K^{\text{u}} = 130 \, \text{kJ m}^{-3}$. The interfacial-type DMI constant D_{int} was tuned to obtain the isolated field-induced Néel-type skyrmion phase without admixtures of maze domains. The minimal value of DMI required for the purely Néel-type skyrmion stability was found to be $D_{\text{int}} = 0.0015 \, \text{J m}^{-2}$. It is remarkable that this value amounts about 8% of the exchange energy of DyCo3[68], in agreement with the suggestion of up to ~20% of the isotropic exchange expected for DMI in disordered systems[69,70] (see Supplementary Note 6).

Data availability

The data that support the findings of this study are available from the corresponding author upon reasonable request.

References

1. Skyrme, T. H. R. A unified field theory of mesons and baryons. *Nucl. Phys.* **31**, 556–569 (1962).
2. Roessler, U. K., Bogdanov, A. & Pfleiderer, C. Spontaneous skyrmion ground states in magnetic metals. *Nature* **442**, 797–801 (2006).
3. Yu, X. et al. Real-space observation of a two-dimensional skyrmion crystal. *Nature* **465**, 901–904 (2010).
4. Münzer, W. et al. Skyrmion lattice in the doped semiconductor Fe₁₋ₓCoₓSi. *Phys. Rev. B* **81**, 041203 (2010).
5. Sampaio, J., Cros, V., Rohart, S., Thiaville, A. & Fert, A. Nucleation, stability and current-induced motion of isolated magnetic skyrmions in nanostructures. *Nat. Nanotechnol.* **8**, 839–844 (2013).
6. Fert, A., Reyren, N. & Cros, V. Magnetic skyrmions: advances in physics and potential applications. *Nat. Rev. Mater.* **2**, 17031 (2017).
7. Parkin, S. S., Hayashi, M. & Thomas, L. Magnetic domain-wall racetrack memory. *Science* **320**, 190–194 (2008).
8. Fert, A., Cros, V. & Sampaio, J. Skyrmions on the track. *Nat. Nanotechnol.* **8**, 152–156 (2013).
9. Parkin, S. & Yang, S.-H. Memory on the racetrack. *Nat. Nanotechnol.* **10**, 195–198 (2015).
10. Zhang, X. et al. Skyrmion-skyrmion and skyrmion-edge repulsions in skyrmion-based racetrack memory. *Sci. Rep.* **5**, 1–6 (2015).
11. Tomasello, R. et al. A strategy for the design of skyrmion racetrack memories. *Sci. Rep.* **4**, 1–7 (2014).
12. Kang, W. et al. Voltage controlled magnetic skyrmion motion for racetrack memory. *Sci. Rep.* **6**, 1–11 (2016).
13. Tomasello, R. et al. Performance of synthetic antiferromagnetic racetrack memory: domain wall versus skyrmion. *J. Phys. D Appl. Phys.* **50**, 325302 (2017).
14. Zhang, X. et al. Skyrmion-electronics: writing, deleting, reading and processing magnetic skyrmions toward spintronic applications. *J. Phys. Condens Matter* **32**, 143001 (2020).
15. Hoffmann, M., Müller, G. P., Melcher, C. & Blügel, S. Skyrmion-antiskyrmion racetrack memory in rank-one dmi materials. *Front. Phys.* **9**, 668 (2021).
16. One, R.-A. et al. Micromagnetic design of skyrmionic materials and chiral magnetic configurations in patterned nanostructures for neuromorphic and qubit applications. *Nanomaterials* **12**, 4411 (2022).
17. Skyrme, T. H. R. A non-linear field theory. *Proc. R. Soc. Lond. Ser. A. Math. Phys. Sci.* **260**, 127–138 (1961).
18. Bogdanov, A. N. & Yablonskii, D. A. Thermodynamically stable "vortices" in magnetically ordered crystals. the mixed state of magnets. *Sov. Phys. JETP* **68**, 101 (1989).
19. Mühlbauer, S. et al. Skyrmion lattice in a chiral magnet. *Science* **323**, 915–919 (2009).
20. Bogdanov, A. & Hubert, A. Thermodynamically stable magnetic vortex states in magnetic crystals. *J. Magn. Magn. Mater.* **138**, 255–269 (1994).
21. Seki, S., Yu, X. Z., Ishiwata, S. & Tokura, Y. Observation of skyrmions in a multiferroic material. *Science* **336**, 198–201 (2012).
22. Neubauer, A. et al. Topological hall effect in the a phase of mnsi. *Phys. Rev. Lett.* **102**, 186602 (2009).
23. Onose, Y., Okamura, Y., Seki, S., Ishiwata, S. & Tokura, Y. Observation of magnetic excitations of skyrmion crystal in a helimagnetic insulator Cu₂OSeO₃. *Phys. Rev. Lett.* **109**, 037603 (2012).
24. Pöllath, S. et al. Ferromagnetic resonance with magnetic phase selectivity by means of resonant elastic x-ray scattering on a chiral magnet. *Phys. Rev. Lett.* **123**, 167201 (2019).
25. Ukleev, V. et al. Chiral surface spin textures in Cu₂OSeO₃ unveiled by soft x-ray scattering in specular reflection geometry. *Sci. Technol. Adv. Mater.* **23**, 682–690 (2022).
26. Yu, X. et al. Near room-temperature formation of a skyrmion crystal in thin-films of the helimagnet fege. *Nat. Mater.* **10**, 106–109 (2011).
27. Heinze, S. et al. Spontaneous atomic-scale magnetic skyrmion lattice in two dimensions. *Nat. Phys.* **7**, 713–718 (2011).
28. Bode, M. et al. Chiral magnetic order at surfaces driven by inversion asymmetry. *Nature* **447**, 190–193 (2007).
29. Yu, G. et al. Room-temperature creation and spin–orbit torque manipulation of skyrmions in thin films with engineered asymmetry. *Nano Lett.* **16**, 1981–1988 (2016).
30. Jiang, W. et al. Blowing magnetic skyrmion bubbles. *Science* **349**, 283–286 (2015).
31. Romming, N. et al. Writing and deleting single magnetic skyrmions. *Science* **341**, 636–639 (2013).
32. Moreau-Luchaire, C. et al. Additive interfacial chiral interaction in multilayers for stabilization of small individual skyrmions at room temperature. *Nat. Nanotechnol.* **11**, 444–448 (2016).
33. Woo, S. et al. Observation of room-temperature magnetic skyrmions and their current-driven dynamics in ultrathin metallic ferromagnets. *Nat. Mater.* **15**, 501–506 (2016).
34. Woo, S. et al. Spin-orbit torque-driven skyrmion dynamics revealed by time-resolved x-ray microscopy. *Nat. Commun.* **8**, 1–8 (2017).
35. Hrabec, A. et al. Current-induced skyrmion generation and dynamics in symmetric bilayers. *Nat. Commun.* **8**, 1–6 (2017).
36. Boulle, O. et al. Room-temperature chiral magnetic skyrmions in ultrathin magnetic nanostructures. *Nat. Nanotechnol.* **11**, 449–454 (2016).
37. Buhrandt, S. & Fritz, L. Skyrmion lattice phase in three-dimensional chiral magnets from monte carlo simulations. *Phys. Rev. B* **88**, 195137 (2013).
38. Ma, M., Pan, Z. & Ma, F. Artificial skyrmion in magnetic multilayers. *J. Appl. Phys.* **132**, 043906 (2022).
39. Jiang, W. et al. Direct observation of the skyrmion Hall effect. *Nat. Phys.* **13**, 162–169 (2017).
40. Litzius, K. et al. Skyrmion Hall effect revealed by direct time-resolved x-ray microscopy. *Nat. Phys.* **13**, 170–175 (2017).
41. Radu, F. & Sánchez-Barriga, J. in (eds.) *Novel Magnetic Nanostructures, Advanced Nanomaterials* (eds Domracheva, N., Caporali, M. & Rentschler, E.) Ch. 9 (Elsevier, 2018).
42. Kim, S. K. et al. Ferrimagnetic spintronics. *Nat. Mater.* **21**, 24–34 (2022).
43. Sala, G. & Gambardella, P. Ferrimagnetic dynamics induced by spin-orbit torques. *Adv. Mater. Interfaces* **9**, 2201622 (2022).
44. Chen, K. et al. Observation of compact ferrimagnetic skyrmions in DyCo₃ film. *Nanoscale* **12**, 18137–18143 (2020).
45. Kim, D.-H. et al. Bulk Dzyaloshinskii–Moriya interaction in amorphous ferrimagnetic alloys. *Nat. Mater.* **18**, 685–690 (2019).
46. Woo, S. et al. Current-driven dynamics and inhibition of the skyrmion Hall effect of ferrimagnetic skyrmions in GdFeCo films. *Nat. Commun.* **9**, 1–8 (2018).
47. Wu, H. et al. Ferrimagnetic skyrmions in topological insulator/ferrimagnet heterostructures. *Adv. Mater.* **32**, 2003380 (2020).
48. Brandão, J., Dugato, D. A., Puydinger dos Santos, M. V. & Cezar, J. C. Evolution of zero-field ferrimagnetic domains and skyrmions in exchange-coupled Pt/CoGd/Pt confined nanostructures: Implications for antiferromagnetic devices. *ACS Appl. Nano Mater.* **2**, 7532–7539 (2019).
49. Wang, X. et al. Topological spin memory of antiferromagnetically coupled skyrmion pairs in co/gd/pt multilayers. *Phys. Rev. Mater.* **6**, 084412 (2022).
50. Brandão, J., Dugato, D., Puydinger dos Santos, M., Béron, F. & Cezar, J. Tuning isolated zero-field skyrmions and spin spirals at room-temperature in synthetic ferrimagnetic multilayers. *Appl. Surf. Sci.* **585**, 152598 (2022).
51. Budhani, R. C. et al. Magnetotransport and magnetic textures in Ho/FeCoGd/β-w multilayers. *Phys. Rev. B* **105**, 024412 (2022).
52. Streubel, R. et al. Experimental evidence of chiral ferrimagnetism in amorphous gdco films. *Adv. Mater.* **30**, 1800199 (2018).
53. Seng, B. et al. Direct imaging of chiral domain walls and Néel-type skyrmionium in ferrimagnetic alloys. *Adv. Funct. Mater.* **31**, 2102307 (2021).

54. Xu, T. et al. Imaging the spin chirality of ferrimagnetic Néel skyrmions stabilized on topological antiferromagnetic Mn_3Sn. *Phys. Rev. Mater.* **5**, 084406 (2021).

55. Büttner, F., Lemesh, I. & Beach, G. S. Theory of isolated magnetic skyrmions: from fundamentals to room temperature applications. *Sci. Rep.* **8**, 1–12 (2018).

56. Legrand, W. et al. Hybrid chiral domain walls and skyrmions in magnetic multilayers. *Sci. Adv.* **4**, eaat0415 (2018).

57. Thole, B., Van der Laan, G. & Sawatzky, G. Strong magnetic dichroism predicted in the m 4, 5 x-ray absorption spectra of magnetic rare-earth materials. *Phys. Rev. Lett.* **55**, 2086 (1985).

58. Kuiper, P., Searle, B. G., Rudolf, P., Tjeng, L. & Chen, C. X-ray magnetic dichroism of antiferromagnet Fe_2O_3: the orientation of magnetic moments observed by Fe 2p x-ray absorption spectroscopy. *Phys. Rev. Lett.* **70**, 1549 (1993).

59. Kortright, J., Kim, S.-K., Ohldag, H., Meigs, G. & Warwick, A. Magnetization imaging using scanning transmission x-ray microscopy. In *AIP Conference Proceedings, Vol. 507* 49–54 (American Institute of Physics, 2000).

60. Schütz, G. et al. Absorption of circularly polarized x rays in iron. *Phys. Rev. Lett.* **58**, 737 (1987).

61. Luo, C., Ryll, H., Back, C. H. & Radu, F. X-ray magnetic linear dichroism as a probe for non-collinear magnetic state in ferrimagnetic single layer exchange bias systems. *Sci. Rep.* **9**, 18169 (2019).

62. Vansteenkiste, A. et al. The design and verification of mumax3. *AIP Adv.* **4**, 107133 (2014).

63. Lemesh, I. & Beach, G. S. Twisted domain walls and skyrmions in perpendicularly magnetized multilayers. *Phys. Rev. B* **98**, 104402 (2018).

64. Birch, M. et al. History-dependent domain and skyrmion formation in 2d van der Waals magnet Fe_3GeTe_2. *Nat. Commun.* **13**, 1–11 (2022).

65. Buhl, P. M. *Topological Transport in Non-Abelian Spin Textures from First Principles*. PhD thesis, RWTH Aachen, Diss. (2019).

66. Nolle, D. et al. Note: Unique characterization possibilities in the ultra high vacuum scanning transmission x-ray microscope (uhv-stxm) "maxymus" using a rotatable permanent magnetic field up to 0.22 t. *Rev. Sci. Instrum.* **83**, 046112 (2012).

67. Ohresser, P. et al. Deimos: a beamline dedicated to dichroism measurements in the 350–2500 eV energy range. *Rev. Sci. Instrum.* **85**, 013106 (2014).

68. Yakinthos, J. K. & Mentzafos, D. E. Neutron-diffraction study of ferrimagnetic $DyCo_3$. *Phys. Rev. B* **12**, 1928–1932 (1975).

69. Fert, A. & Levy, P. M. Role of anisotropic exchange interactions in determining the properties of spin-glasses. *Phys. Rev. Lett.* **44**, 1538 (1980).

70. Fert, A. in *Metallic Multilayers, Vol. 59 of Materials Science Forum* 439–480 (Trans Tech Publications Ltd, 1990).

Author contributions

C.L., K.C., and F.R. conceived and designed the experiments. K.C. prepared the samples. C.L. and F.R. performed the STXM experiments with the help of S.W. and M.W.; C.L. and K.C. analyzed the STXM data and prepared the figures. V.U. performed the micromagnetic simulations. K.P. performed the magnetic characterization by SQUID. R.-M.A., C.L., V.U. and F.R. performed the magneto-transport experiments. C.L., V.U. and F.R. wrote the manuscript draft. All authors discussed the results and contributed to the manuscript.

Competing interests

The authors declare no competing interests.

Additional information

Supplementary information The online version contains supplementary material available at https://doi.org/10.1038/s42005-023-01341-7.

Correspondence and requests for materials should be addressed to Kai Chen or Florin Radu.

Peer review information *Communications Physics* thanks the anonymous reviewers for their contribution to the peer review of this work.

Reprints and permission information is available at http://www.nature.com/reprints

Publisher's note Springer Nature remains neutral with regard to jurisdictional claims in published maps and institutional affiliations.